Research Square

Preprints are preliminary reports that have not undergone peer review.
They should not be considered conclusive, used to inform clinical practice,
or referenced by the media as validated information.

Changing the Cross-Sectional Shapes of the Prestressed Rovings in Warp-Knitted Glass and Carbon Reinforcing Fabrics

Oleg Stolyarov

stolyarov_on@spbstu.ru

Peter the Great St. Petersburg Polytechnic University

Pavel Mostovykh

Peter the Great St. Petersburg Polytechnic University

Research Article

Keywords: cross-sectional shape, high-strength rovings, reinforcing fabrics, prestress, fiber distribution

Posted Date: November 2nd, 2026

DOI: https://doi.org/10.21203/rs.3.rs-11404913/v1

License: This work is licensed under a Creative Commons Attribution 4.0 International License.
Read Full License

Additional Declarations: No competing interests reported.

CHANGING THE CROSS-SECTIONAL SHAPES OF THE PRESTRESSED ROVINGS IN WARP-KNITTED GLASS AND CARBON REINFORCING FABRICS

Oleg Stolyarov[1] *** and Pavel Mostovykh**

Peter the Great St.Petersburg Polytechnic University

Keywords: cross-sectional shape; high-strength rovings; reinforcing fabrics; prestress; fiber distribution

Abstract: Understanding the changes in the reinforcing fabrics during loading is an urgent task, as it provides the necessary information for predicting the mechanical behaviors of fabrics and fabric-based composites. The effect of the loading level on the internal structure of the reinforcing fabrics was evaluated through the experimental studies on samples of warp-knitted glass and carbon reinforcing fabrics with different stitch patterns, including tricot and pillar stitches. To establish relationships between the changes in the roving cross-section during loading, optical microscopy was used. Several prestressed levels corresponding to 0%, 25%, 50%, and 75% of the tensile strength of the reinforcing fabric were analyzed. Based on the constructed geometrical models, a statistical analysis of fiber distribution was carried out. With increasing loading, the cross-sectional shape changes significantly in the case of the tricot stitch. In contrast to the fabric with tricot stitch, the cross-sectional shape of the fabric with pillar stitch slightly decreases with an increase in the applied load.

1. Introduction

Prestressed concrete finds widespread application in construction. Unlike simple reinforced concrete, prestressed concrete possesses less deflection and high crack resistance [1]. The use of high-strength textiles in prestressed concrete has elicited an increased interest in the last two decades as well [2-7]. These types of reinforcement are corrosion-free and allow to develop thin and light weight structural elements [8-12].

Various textile fabrics and meshes including woven and warp-knitted are used for prestressing. Warp-knitted fabrics with mesh-like, open structures as reinforcing structures composed of glass or carbon rovings have attracted considerable attention [13-17]. In the warp-knitted fabrics, high-strength rovings are inserted in the 0^o and 90^o directions and then combined by polyester yarn. The reinforcing rovings consist of thousands of filaments. Various types of warp-knitted stitches, including tricot (see Fig. 1a) and pillar (see Fig. 1b) can be used. The stitch type determines the geometry of the internal structure of the warp-knitted fabric and its tensile behavior.

[1] Corresponding author

Oleg Stolyarov

29, Polytechnicheskaya, St.Petersburg, 195251, Russia

stolyarov_on@spbstu.ru

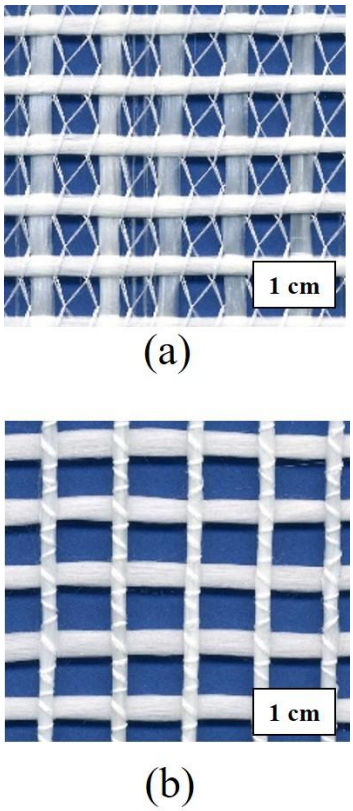


Fig. 1. Structures of warp-knitted reinforcing fabrics with different stitch types.

Understanding the deformation mechanics of textile reinforcing materials is fundamental to establishing the relationship between the structure and mechanical behaviors. Analysis of the changes in the fabric internal geometry including the redistribution of the fibers within the rovings and contact length of the roving is very valuable as regards modeling of the reinforcing fabrics and cement-based composite properties. The study of the relationships between the structures and properties of warp-knitted fabrics for technical purposes is of great interest, owing to the possibility of evaluating such structures in regard to sustaining mechanical loading. Technical warp-knitted fabrics are used in many application areas, and unlike conventional fabrics, they have a higher surface density and thickness. These fabrics are made of high-performance rovings with a high linear density reaching 1600–2400 tex. Such rovings contain several thousand individual filaments in their cross-sections. The mechanism of their interaction is somewhat different when compared with a synthetic yarn consisting of several dozens of filaments. The main reason for this is the friction between the filaments, which work differently in the inner and outer layers. This determines the shape of the reinforcing roving, which has a definite effect on strength efficiency. Xu et al. [18] investigated the bond characteristics of reinforcing textiles in mortar. Unlike steel reinforcement, the cross-section of reinforcing rovings in textiles can significantly change.

The effects of applied pretension on warp-knitted fabrics during the production of fiber-reinforced cement composites have been investigated in detail [7, 18-20]. In these studies, the prestress levels ranged from 12.5 to 35 %. It has been found that prestressing of textiles significantly affects the mechanical performance of reinforced concrete. However, some differences have been found in the application of various fiber types. Investigation of structure's relationship under loading is very valuable, as the results can be used in the modeling of the mechanical behavior under various loading conditions. Some authors have attempted to carry out the analysis of the prestressed

textile-reinforced concrete. In most cases, levels up to 35% of the maximum tensile strength are selected for the prestressing study of textile reinforcement.

The cross-sectional shape of the yarn significantly affects both the properties of the reinforcing fabrics and the properties of the concrete composites. In Ref. [21], the yarn cross-sectional shape in a woven fabric was considered. The cross-sectional shapes were found different during weaving and after removal. Some authors carried out experiments on simultaneous loading of textiles and analysis of changes in the cross-sections within the textile. Optical microscopy [22- 24] as well as computer tomography [7, 25, 26] are used to analyze changes in the cross-sectional shapes of textiles. In Ref. [7], changes in the roving cross-sectional shape in a warp-knitted fabric during prestress were analyzed. It was shown that there is a relationship between the characteristics of the cross-sectional shape of the roving and the flexural properties of concrete composites reinforced with these rovings. Increase in the contact length, as well as the average radius of the fiber distribution within the roving cross-section, directly affects the increase in the flexural strength of the prestressed concrete composite. Changing in the shape of the roving cross-section due to variation in the internal structure, for example, in a non-prestressed concrete composite, also affects the flexural properties. The key factor is changing the cross-sectional shape and its geometric parameters, including the contact length and the average radius of fibers. The fabric construction based on the stitch type significantly affects its tensile properties and the properties of the cement-based composites.

To the best of our knowledge, studies on the influence of loading on the roving properties are very few in the literature. The aim of this work is to evaluate changes in characteristics of the prestressed rovings in warp-knitted reinforcing fabrics, and to establish the relationship between the pre-stress level and the roving geometry. The analysis is based on an examination of the roving cross-sectional shape of variation as a function of the prestressing.

2. Materials and Methods

2.1. Materials

Warp-knitted fabrics with different characteristics were used in this study. Table 1 lists the main structural characteristics of the warp-knitted fabrics. was used as the knitting yarn.

TABLE 1. Sample specifications

Series	Sample designation	Fabric construction			Pattern
		Warp inlay roving	Weft inlay roving	Knitting yarn	
1	GR-T	AR-glass rovings, 2400 Tex	AR-glass rovings, 2400 Tex	Polyester multifilament yarn, 16.7 Tex	Tricot
2	GR-P				Pillar
3	CR-T	Carbon rovings, 24K, PAN-based, 1600 Tex			Tricot
4	CR-P				Pillar

2.2. Methods

2.2.1 Loading

In Fig. 2, a universal testing machine model Instron 5965 for prestressing fabric is presented. To test the fabric samples, the ends of the specimen were fixed in the clamps and extended to various loading levels corresponding to 0% (an initial un-extended state), 25%, 50%, and 75% of the maximal tensile strength of the fabric (σ_{max}). After stopping the testing machine, the fast-hardening cyanoacrylate resin was applied on the specimen surface to fix a deformed structure. At least three measurements were performed at each loading level. The fixed square area of 30 × 30 mm was then cut. The fabric cross-sections were examined by optical analysis.

Tensile stress was determined using the following equation

$$\sigma = \frac{F\rho}{Tn} \tag{1}$$

where F is the maximal applied force (N), ρ is roving density (kg/m^3), T is the nominal linear density of the roving (Tex) and n is a number of rovings in the fabric cross-section.

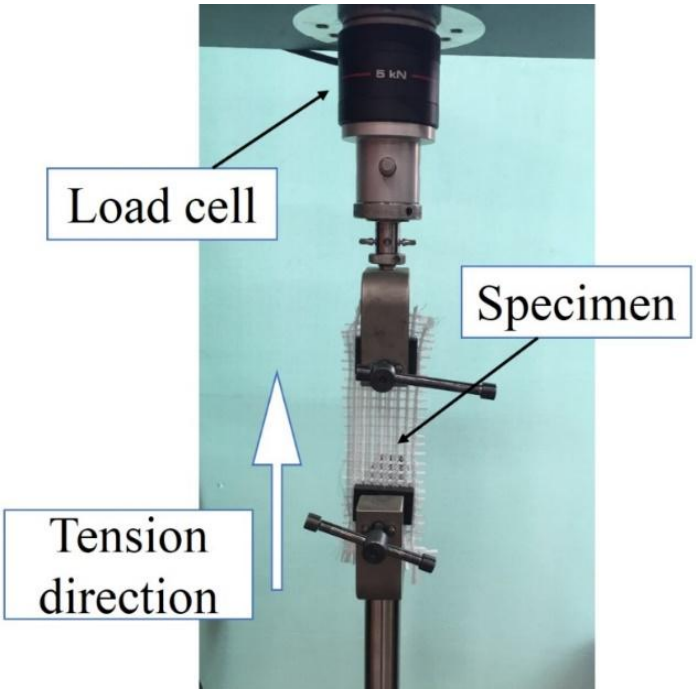


Fig. 2. Experimental setup for analysis of warp-knitted fabric during loading.

2.2.2. Analysis of the roving cross-section

To determine the changes in the cross-sectional shape after prestressing, an analysis of the roving cross-sectional shape was performed using an optical microscope with a digital camera. Optical micrographs of the cross-sections were obtained and recognized in accordance with [7]. The fabric samples were examined at four loading levels in the initial (reference) and prestressed states. Within each fabric sample, at least three rovings were selected for analysis. Optical micrographs were taken on separate rovings.

The procedure of micrograph processing of a roving sample is shown in Fig. 3. The original image of a roving sample is shown in Fig. 3a. Then, image pre-processing was carried out. Gray-level values were rescaled

and binarized. The fibers were distinguished from the background recognised. The recognized fibers in a coordinate system are shown in Fig. 3b.

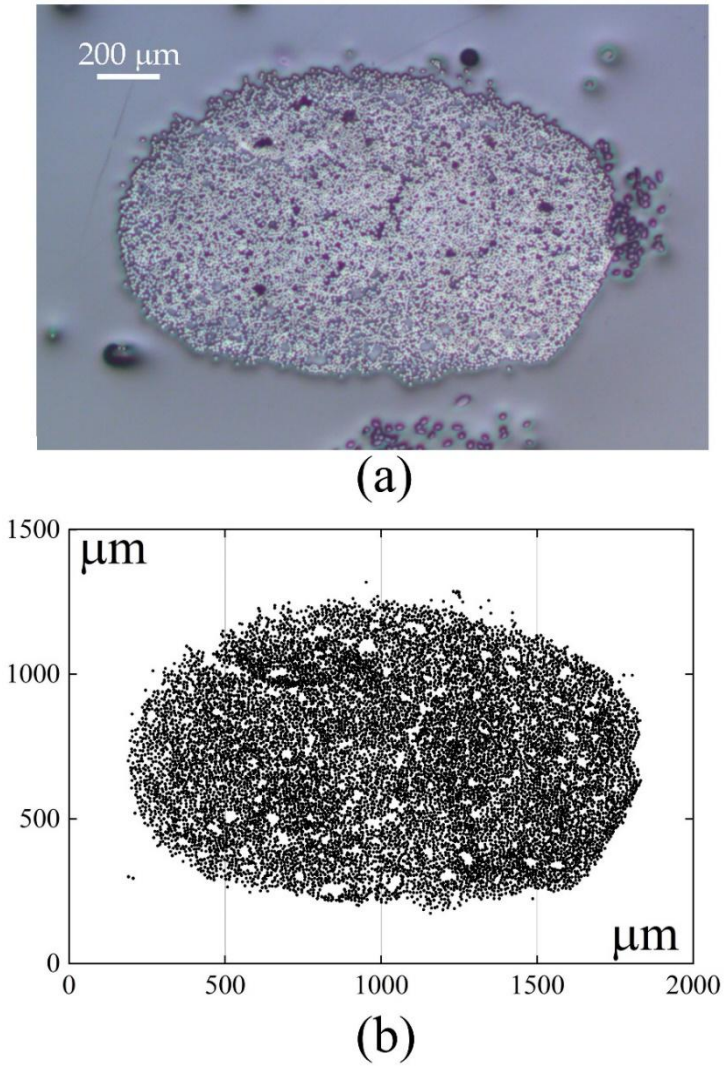


Fig. 3. (a) Micrograph of cross-section and (b) recognized fibers in a coordinate system.

To characterize the changes in the cross-sectional shape of the roving, the statistical analysis of the roving cross-section was done. Additionally, the contact length was defined as a perimeter of the roving cross-section.

3. Results and discussion

3.1 Tensile properties

Tensile tests of two fabric samples were performed using a universal testing system, Instron 5965. Fig. 4 shows the tensile stress–strain curves of the two material samples. It can be observed that the tensile strength of the carbon fabric is nearly twice that of the glass reinforcing fabric. Based on the obtained tensile diagrams, the stress levels at which micrographs were taken were calculated. The strength of the glass roving fabric is 890 MPa, and the strength of the carbon roving fabric is 1865 MPa. The preload levels were calculated from these values, which were 222, 445 and 668 MPa for glass roving and 466, 932 and 1400 MPa for carbon roving.

+

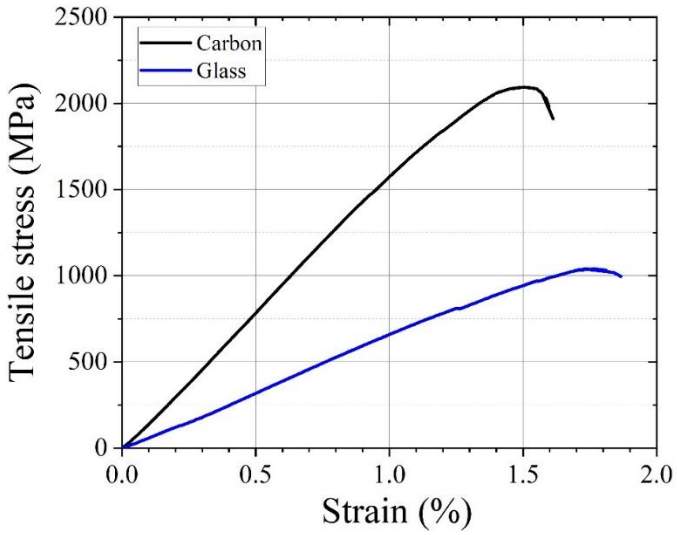


Fig.4. Stress-strain curves of warp-knitted fabrics made of glass and carbon rovings.

3.2 Analysis of the roving cross-section during loading

The warp-knitted fabric samples were tested for two stitch patterns. The cross-section of tricot stitch has a hemi-elliptical shape, and the pillar stitch acquires almost circular shape. Figs. 5 and 6 show the micrographs of the cross-section of glass and carbon rovings, respectively. On the left side, the cross-sections of tricot stitch are shown, on the right side for the chain stitch. Figs. (a) and (b) show the initial reference state of the rovings. Further, Figs. of the prestressed rovings are shown. Figs. (c) and (d) correspond to a prestress level of 25%. Figs. (e) and (f) correspond to a prestress level of 50% and Figs. (g) and (h) correspond to a prestress level of 75% of the tensile strength.

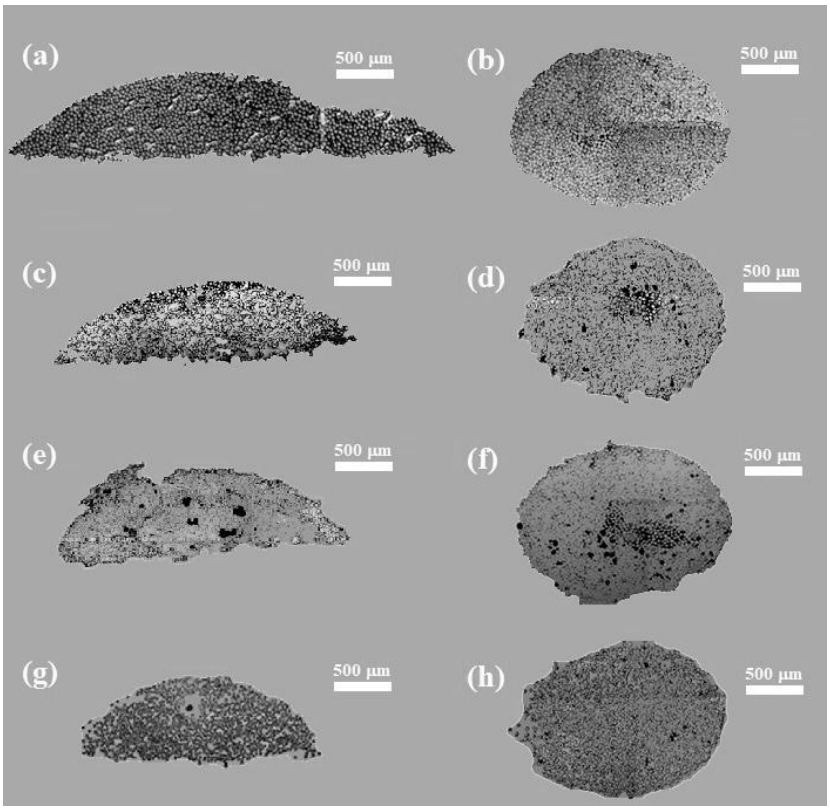


Fig. 5. Cross-sections of glass roving in warp-knitted fabric of tricot stitch (left) and pillar stitch (right).

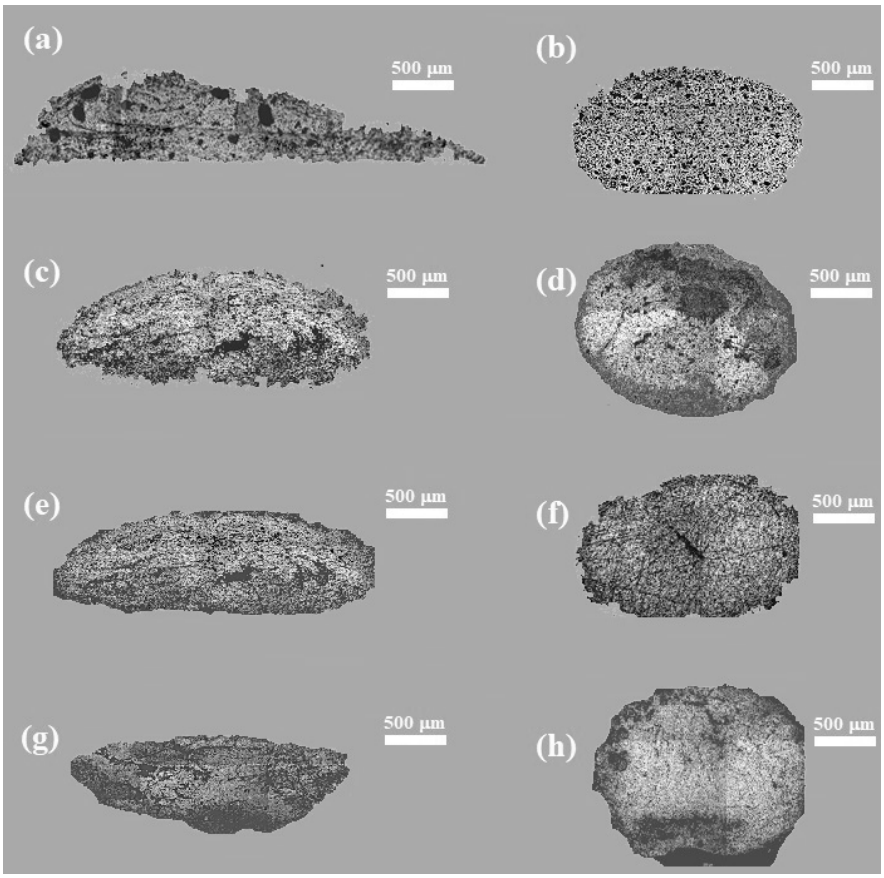


Fig. 6. Cross-sections of carbon roving in warp-knitted fabric of tricot stitch (left) and pillar stitch (right).

3.2. Geometric models

Geometric models of the roving cross-sections are shown in Fig. 7. On the left side are samples with a tricot stitch, and on the right, a pillar stitch. In the initial "static" state (0%), the reinforcing roving with a tricot stitch has a flattened shape with the maximum filament distribution and greatest contact length. The samples of rovings from fabrics with a pillar stitch have a circular shape. Furthermore, with an increase in the load to 25% of σ_{max}, the shape of the roving starts to change. For the tricot stitch, the cross-sectional area is somewhat reduced, while maintaining a shape similar to that in the static state. For the pillar stitch, the cross-section is reduced in diameter. Upon reaching the levels of 50% and 75% of σ_{max} in the case of the tricot stitch, the cross-sectional shape changes significantly. The flattening of the roving is significantly reduced, its length is significantly reduced; in contrast, the height increases. The filaments are grouped closer to the cross-section center. The roving itself tends to take a shape close to circular. This explains the interaction with the weft rovings, which, owing to the compressive forces, lead to the decrease in its dimensions. For the pillar stitch, the cross-sectional shape remains circular, independent of the loading level. In this case, a slight decrease in diameter is observed; this is also caused by the migration of filaments to the cross-section center of gravity. Summarizing the above, we can conclude that the changes in the roving cross-sectional shape depend significantly on the level of the applied load, especially in the initial stages of deformation (up to 25%).

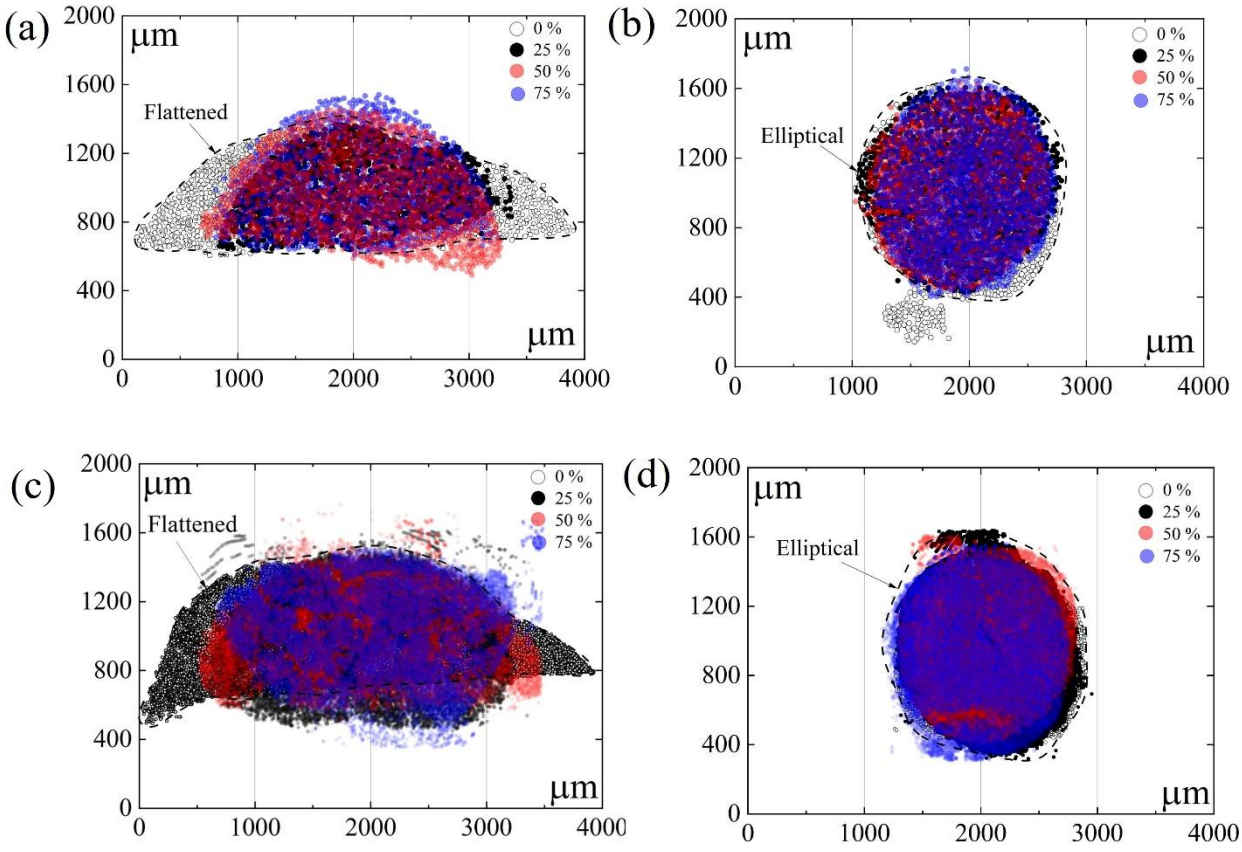


Fig. 7. Resulting recognized models of cross-sections of glass (a and b) and carbon (c and d) rovings in warp-knitted fabric of tricot stitch (left) and pillar stitch (right).

3.3. Contact length

To clearly characterize the changes in the roving cross-section depending on the loading stage, the contact length is calculated (Eq. 2). The main idea of plotting such a relationship is to identify the magnitude of the critical changes in the size of the roving cross-section. This is extremely important as, for example, a sharp decrease in contact length can lead to a loss of bond between reinforcement and concrete. Dependence of contact length of the roving depending on the prestress level is shown in Fig. 8. It is clearly seen that in all cases, these parameters decrease sharply in the range of 0 to 25% of σ_{max}. Furthermore, the size of the cross-sectional shape changes less significantly. The curve reaches a plateau.

To determine the critical value of the prestress based on the decreasing dependence of the contact length and average radius thereon, a corresponding method is proposed. The indicated dependences are analytically convenient to set as follows

$$l_{ct} = l_{\infty} + (l_0 - l_{\infty})e^{-t/t_s}, \tag{2}$$

where l_{ct} is the contact length (mm); l_0, l_{∞}, are the initial and final values of the contact length; t is the pre-tension; and t_s is the pretensioning value (exponential parameter) characterizing this dependence.

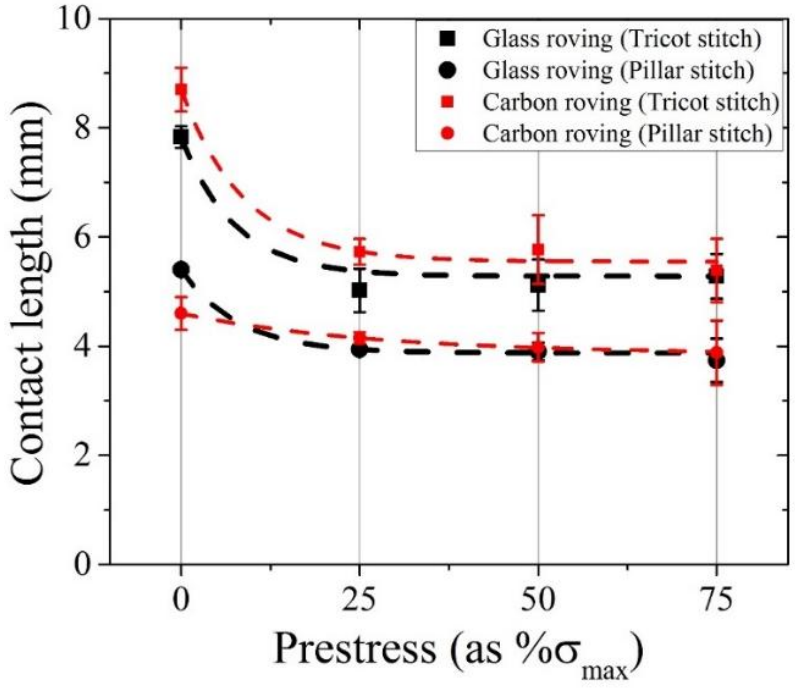


Fig. 8. Dependence of contact length of the roving depending on the prestress level.

Using the exponential parameter in Eq. 2, we can determine the boundaries at which the value of the contact length decreases by a factor of "*e*" (2.7 times). This corresponds to reaching an equilibrium state. Using this dependence, it is possible to determine the critical decrease in one of the parameters of the roving cross-section. This decreasing dependence of the roving cross-section parameter on the pre-tension of the roving can be used to predict the behavior of the roving during the operation or manufacture of products, i.e., by adjusting its pre-tension. This criterion can also be defined as the load boundary between the initial state of the fibers in the roving cross-section and the new rearranged state of the fibers, which is closer to equilibrium. The calculation results are presented in Table 2. According to the data, the tricot stitch shows the strongest effect of the pre-tension on the cross-sectional shape of the prestressed warp-knitted fabric. It turns out that for a fabric with a tricot stitch, the contact length begins to decrease significantly at a maximum level of 7.5–8.8% of σ_{max}. This can be clearly seen from the dashed lines with squares. These characteristics significantly decrease and reach an equilibrium state at a maximum level of 25% of σ_{max}. For fabric with a pillar stitch, this is less significant, as indicated by the dashed lines with circles. A decrease in the characteristic by a factor of "*e*" is shifted to the right of the prestress scale. This parameter decreases by 8% for the carbon roving, whereas it decreases by 27.1% for the carbon roving. This difference can be explained by the different numbers of filaments in the structures of the rovings and their size. There are approximately 1000 individual filaments in the glass roving, whereas there are 24,000 in the structure of the carbon roving. In addition, the filament diameter is of great importance and is three times smaller in the carbon roving.

TABLE 2. Exponential parameters in Eq. 2

Contact length	Glass	7.5	8.0
	Carbon	8.8	27.1

Comparing the two studied stitches and obtained characteristics, the following deformation features can be distinguished. In a roving in a fabric with a tricot stitch, there is a significant and sharp decrease in the calculated characteristics. The contact length decreases by approx. 35–38%. For the pillar stitch, the change in the contact length decreases slightly more, by 25% and 15% for glass and carbon rovings, respectively. This difference in values is evident in Fig. 8. The shape of the roving in the tricot stitch changes significantly; from an elongated narrow shape, it acquires an oval shape. The flattening ratio, the ratio of the minor to major radii, was taken as

$$e = b/a \tag{3}$$

where b – minor radius, a – major radius.

The flattening factor (Eq. 3) increases from 0.2 for the initial state to 0.38 (75% of σ_{max}) for the glass roving and from 0.24 to 0.42 for the carbon roving, i.e. almost double. In contrast, for the pillar stitch, it changes insignificantly, from 0.68 to 0.74 for the glass roving and from 0.66 to 0.78 for carbon roving, i.e. by 10–15%. Notably, for a circular cross-section, the value of this coefficient is equal to one. An increase in this coefficient indicates that the section becomes circular. Moreover, this leads to the worst efficiency in the mechanical properties of the warp-knitted fabrics and items based on them.

Thus, at a prestress of more than 25% of σ_{max}, the calculated characteristics of the cross-sectional shape of the roving cease to depend on a further increase in stress. The migration and rearrangement of individual filaments within the roving occur completely in the first quarter of the loading. Further migration is not possible, owing to constraints with adjacent knitting yarns. When calculating the main parameters of the cross-section of a textile reinforcement, it is recommended to take operational tensile stresses on the order of 15–20% of σ_{max}. Therefore, the parameter 't' of Eq. 2 is proposed to be used as the specified optimum value of prestressing load.

3.4. Statistical analysis

Statistical analysis of the obtained images for each material and each stress level studied was done using the following data:

Standard deviations SD_x, SD_y represent the dispersion in the x and y directions, respectively; they are calculated according to

$$SD_x = \sqrt{\frac{1}{N}\sum_{i=1}^{N}(x_i - c_x)^2}, \tag{4}$$

with c_x the mean value of the x coordinate, $c_x = \frac{1}{N}\sum_{i=1}^{N} x_i$, and similarly for y;

Interquartile ranges IQR_x, IQR_y are evaluated as the difference between the 75% and the 25% largest coordinate values. If the distribution had been Gaussian, then IQR=1.349SD, but in our case the distribution shape is significantly different, with shallower height of the distribution density, and IQR> 1.349SD.

Average radius R of the fiber distribution is evaluated as

$$R = \sqrt{\mathrm{SD}_x^2 + \mathrm{SD}_y^2} \tag{5}$$

for comparison, the values

$$R^* = \frac{1}{N}\sum_{i=1}^{N}\sqrt{\left(x_i - c_x\right)^2 + \left(y_i - c_y\right)^2} \tag{6}$$

proposed as the average radius in [26] are also provided.

The compressive strain values in the x and y directions ε_x, ε_y based on IQR are estimated as

$$\varepsilon_x = 1 - \frac{\mathrm{IQR}_x(\sigma)}{\mathrm{IQR}_x(0)} \tag{7}$$

where the nominator is the IQR value under applied stress σ and the denominator is the IQR value before the stress application, and similarly for y.

Similarly, the compressive strain values in the x and y directions ε_x, ε_y based on SD are estimated as

$$\varepsilon_x = 1 - \frac{\mathrm{SD}_x(\sigma)}{\mathrm{SD}_x(0)} \tag{8}$$

and similarly for y;

The transverse strain ratio ν_x, ν_y are given by

$$\nu_x = \frac{\varepsilon_x}{\varepsilon_z} \tag{9}$$

where ε_z is the tensile strain in the direction of loading, and similarly for y.

Let us note that the proposed transverse strain ratio is a characteristic of the fabric structure rather than of the filament material, and can therefore lie outside the normally adopted range [-1; 0.5].

Fig. 9 shows range-based definition of strain (total Range of variation is used in the same way as SD or IQR). It can be seen that the way strain is defined does not significantly affect the result. As could be expected, the most change occurs at the beginning of loading (between 0 and 25 % of ultimate stress); the only exception is glass tricot in the y direction. The sign on Fig. 9 is positive for compression (and the data shows that in the larger *x* direction the material compresses), whereas it is negative for tension (and the experiment reveals that in the shorter *y* direction the material elongates).

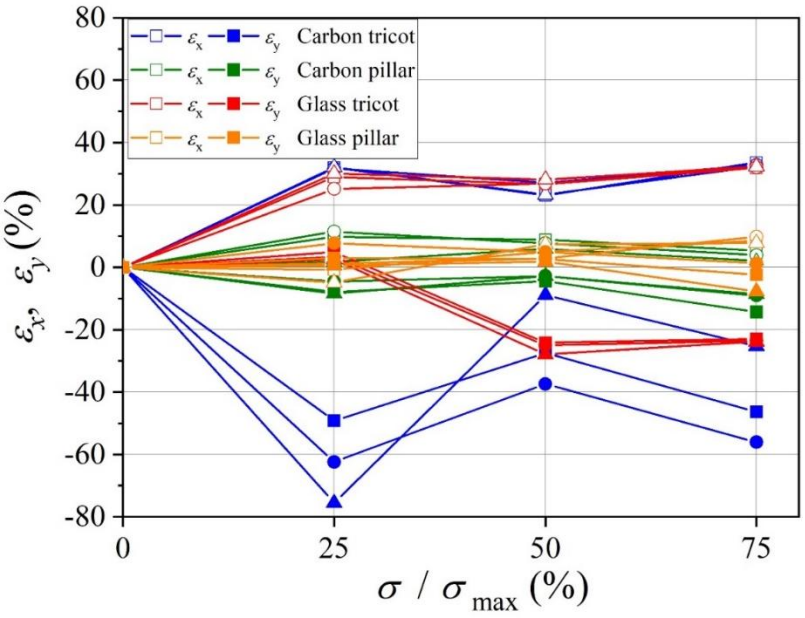


Fig. 9. Dependences of the lateral strains ε_x, ε_y on the relative stress level for the materials tested: SD-based - squares, IQR-based - circles, range-based – triangles.

As long as the way of calculation is of minor importance, Fig. 10 shows the transverse strain ratios only for SD-based calculations. As already mentioned, in fabrics lateral strains are significantly higher than longitudinal, that results in transverse strain ratios of the order 10 and even 100 for carbon tricot at the lowest applied stress level 25 % of the ultimate stress.

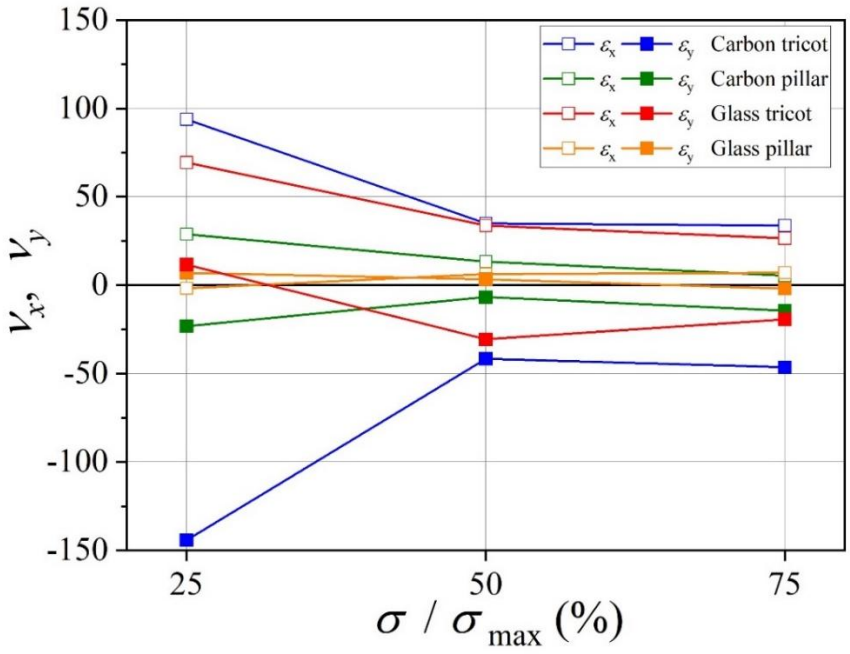


Fig. 10. Dependences of the lateral strains ε_x, ε_y on the relative stress level for the materials tested.

The obtained photographic results, especially for pillar stitch, resemble elliptic shape. To confirm this hypothesis, Figs. 11 and 12 present ellipses described by its equation

$$\left(\frac{x-c_x}{a_x}\right)^2+\left(\frac{y-c_y}{a_y}\right)^2=1 \tag{11}$$

Equation (11) includes four parameters, two of which (c_x and c_y) are coordinates of its center and the other two (a_x and a_y) are its semi-axes. The former two are assigned to the average values, and the origin of coordinates is shifted into that point. The latter two are assigned as half the range in the appropriate axis.

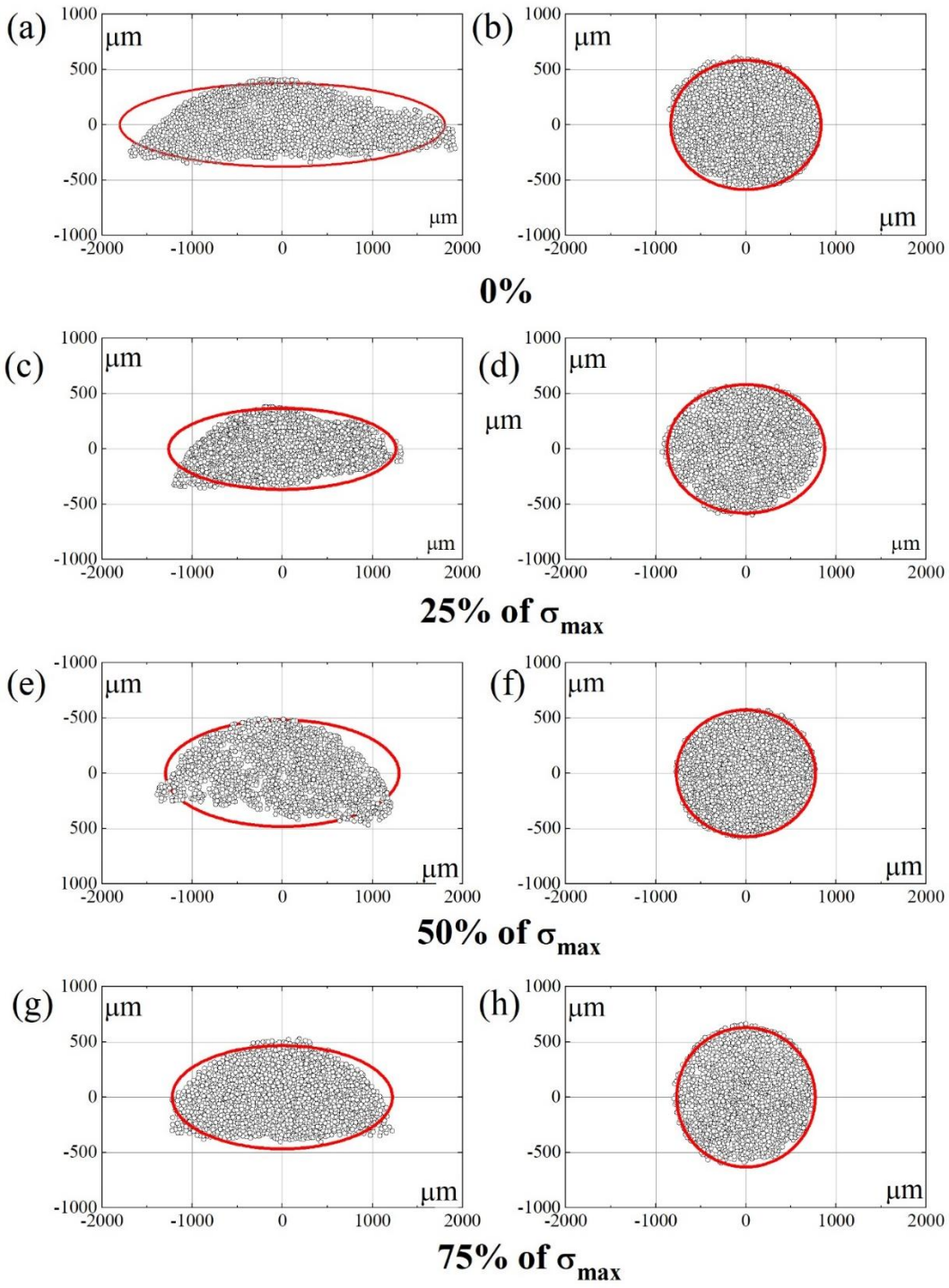


Fig. 11. Ellipse approximations of the obtained fiber distributions for glass.

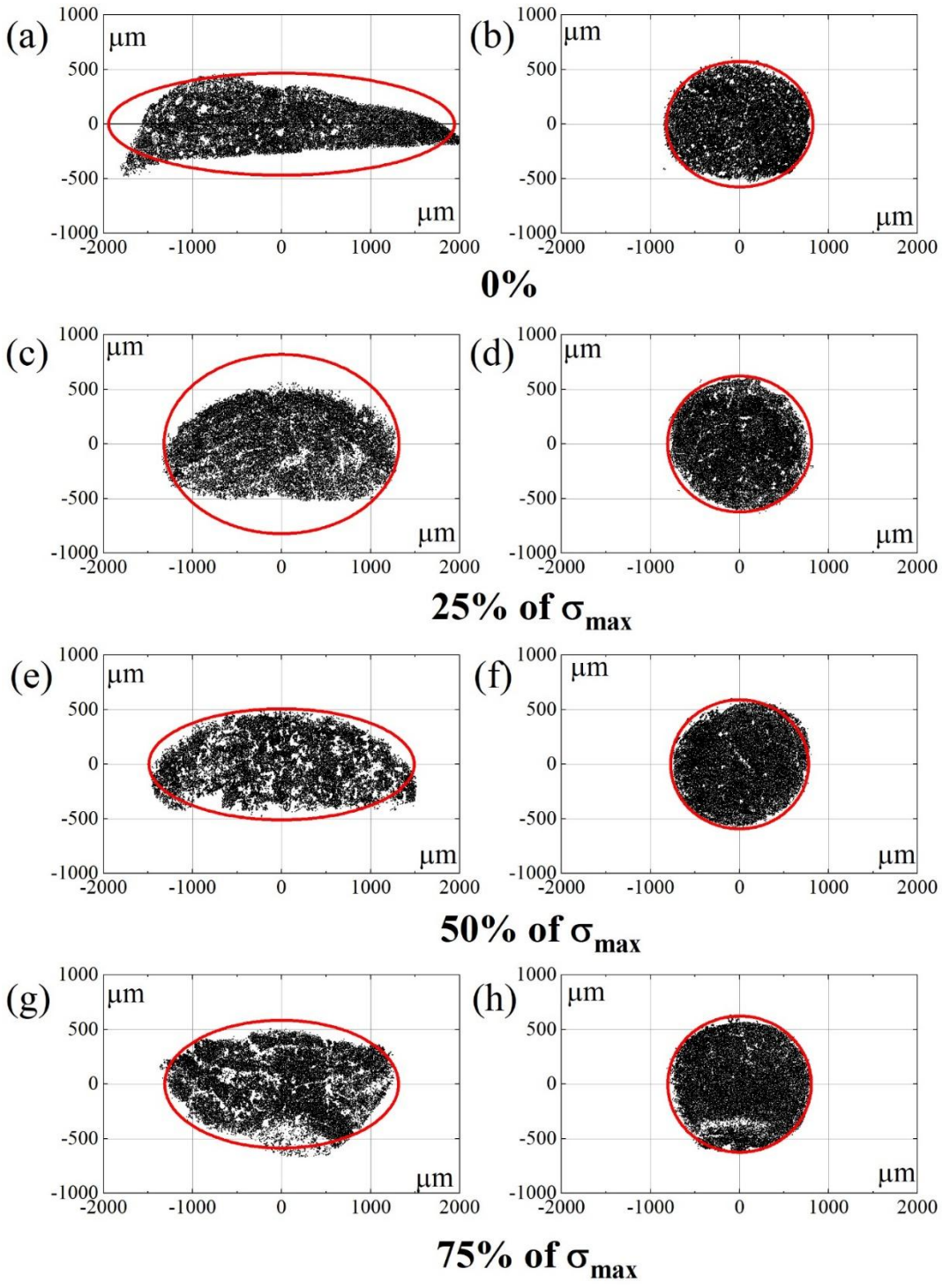


Fig. 12. Ellipse approximations of the obtained fiber distributions for carbon.

Apart from graphical comparison, a number of statistical parameters are also compared between the experimental data and the elliptical model | these include the standard deviation and the quartile values P_{25}, P_{75}. Experimental and theoretical values are compared in Table 2; the theoretical values have been calculated as follows.

For a number of fibers uniformly distributed inside an ellipse (11)

$$\left(\frac{x-c_x}{a_x}\right)^2+\left(\frac{y-c_y}{a_y}\right)^2\le 1 \tag{12}$$

all statistical parameters can be calculated analytically:

$$\mathrm{Mean}_x \equiv \frac{1}{\pi a_x a_y}\int_{c_x-a_x}^{c_x+a_x} x\cdot 2a_y\sqrt{1-\left(\frac{x-c_x}{a_x}\right)^2}\,dx \equiv \frac{2}{\pi}\int_{-\pi/2}^{\pi/2}\left(c_x+a_x\,sin\,\phi\right)cos^2\,\phi d\phi = c_x \tag{13}$$

$$\mathrm{SD}_x^2 \equiv \frac{1}{\pi a_x a_y}\int_{c_x-a_x}^{c_x+a_x}\left(c_x-a_x\right)^2\cdot 2a_y\sqrt{1-\left(\frac{x-c_x}{a_x}\right)^2}\,dx = \frac{2}{\pi}\int_{-\pi/2}^{\pi/2} a_x^2\sin^2\phi\cos^2\phi d\phi = \frac{a_x^2}{4} \tag{14}$$

where the substitute $x = c_x + a_x\sin\phi d\phi$ is used.

Since the area of ellipse corresponding to $x < \tilde{x}$ is given by

$$S = \frac{\pi a_x a_y}{2}+\frac{a_x}{a_y}\left(\left(\tilde{x}-c_x\right)\sqrt{a_x^2-\left(\tilde{x}-c_x\right)^2}+a_x^2\arcsin\frac{\tilde{x}-c_x}{a_x}\right), \tag{15}$$

quartile borders x_{25} and x_{75} are given by

$$-\frac{\pi a_x a_y}{4} = \frac{a_x}{a_y}\left(\left(x_{25}-c_x\right)\sqrt{a_x^2-\left(x_{25}-c_x\right)^2}+a_x^2\arcsin\frac{x_{25}-c_x}{a_x}\right) \tag{16}$$

$$\frac{\pi a_x a_y}{4} = \frac{a_x}{a_y}\left(\left(x_{75}-c_x\right)\sqrt{a_x^2-\left(x_{75}-c_x\right)^2}+a_x^2\arcsin\frac{x_{75}-c_x}{a_x}\right). \tag{17}$$

The corresponding angles are ϕ_{25} = -66.173229^0, ϕ_{75} = 66.173229^0, and the values $x_{25} = c_x$-0.40397276a_x, $x_{75} = cx$ + 0.40397276a_x.

The obtained numerical results confirm visual observation that tricot stitch deviates significantly from elliptic shape (up to 50 % difference between values), whereas pillar stitch deviates within 10 %. This comparison can also be presented in the form of cumulative probabilities or number counts. Figs. 13 and 14 show that for pillar stitch carbon the frequency of small deviations from 0 is underestimated by the theory whereas large deviations from 0 is overestimated. However, both these effects are quantitatively small, making the proposed theory of uniform fiber distribution within an ellipse a reasonable approximation for this material.

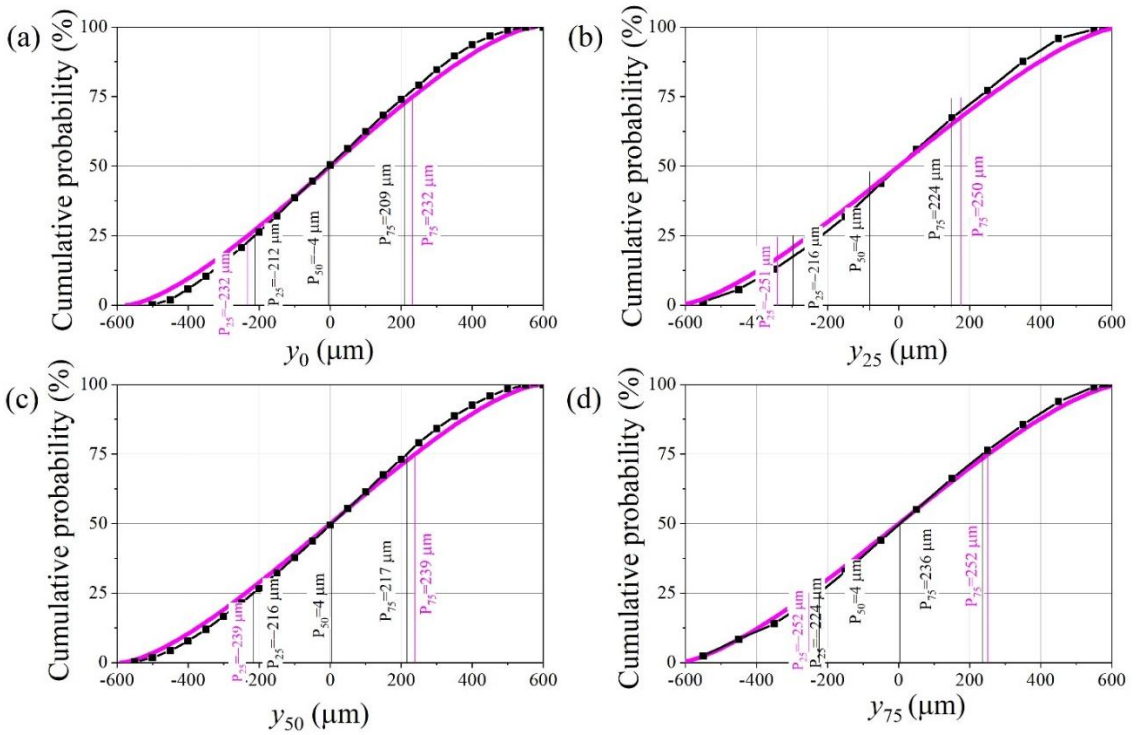


Fig. 13. Cumulative probability of the fiber distribution in tricot stitch carbon in the *y* (shorter) direction. Experiment: black line and dots; theory: magenta. (a): loading 0%; (b): loading 25 %; (c): loading 50 %; (d): loading 75 %.

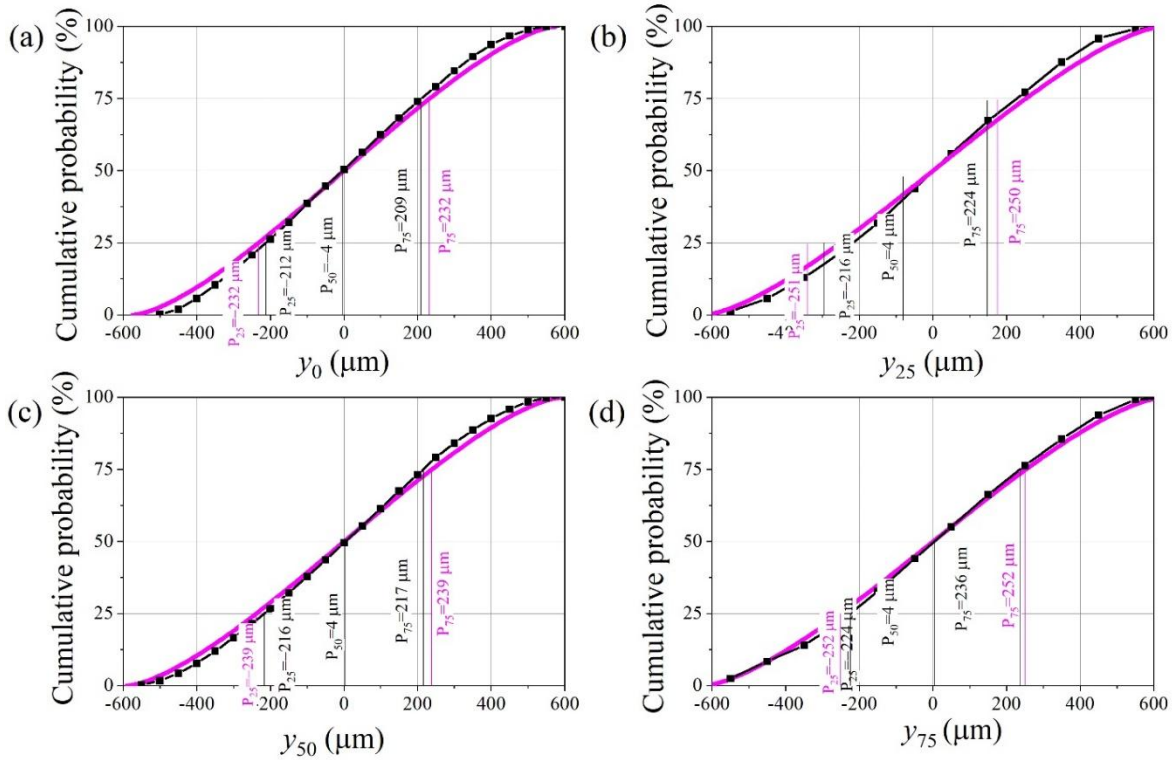


Fig.14. Cumulative probability of the fiber distribution in pillar stitch carbon in the y (shorter) direction. Experiment: black line and dots; theory: magenta. (a): loading 0%; (b): loading 25 %; (c): loading 50 %; (d): loading 75 %.

Table 3 presents further results of statistical analysis of the obtained images.

TABLE 3. Second moments of the fiber distributions.

Material		Stress level	Statistical results			Secondary results		
			Ix, mm^2	Iy, mm^2	Ixy; mm^2	I_1, mm^2	I_2, mm^2	α_0, ^{0}
Glass roving	Tricot stitch	0%	1109	51	1.4	1109	51	-0.1
		25%	559	46	26.5	560	44	-3.0
		50%	596	78	46.1	600	74	-5.0
		75%	514	77	1.0	514	77	-0.1
	Pillar stitch	0%	257	129	-13.9	259	127	6.1
		25%	261	121	12.5	262	120	-5.1
		50%	232	122	17.8	235	119	-9.0
		75%	215	135	7.4	216	134	-5.2
Carbon roving	Tricot stitch	0%	21762	699	-151	21763	697	0.4
		25%	10068	1555	8.2	10068	1555	-0.1
		50%	12871	1135	-109	12872	1134	0.5
		75%	9593	1497	-222	9599	1491	1.6
	Pillar stitch	0%	4049	1580	-157	4059	1570	3.6
		25%	3291	1839	-219	3324	1807	8.4
		50%	3363	1722	241	3398	1687	-8.2
		75%	3624	2063	-183	3645	2042	6.6

Here I_x, I_y are second moments of the cross-section, defined in our case by

$$I_x = \sum_{i=1}^{N} \left(x_i - c_x\right)^2 , \; I_y = \sum_{i=1}^{N} \left(x_i - c_y\right)^2 \tag{18}$$

and that numerically are evaluated based on variation of x_i and y_i, respectively

I_{xy} is the product moment of the cross-section, defined in our case by

$$I_{xy} = \sum_{i=1}^{N} \left(x_i - c_x\right)\left(y_i - c_y\right) \tag{19}$$

that numerically is calculated as a sum of $\left(x_i - c_x\right)\left(y_i - c_y\right)$ values;

I_1, I_2 are main second moments of the cross-section given by

$$I_{1,2} = \frac{1}{2}\left(I_x + I_y \pm \sqrt{\left(I_x - I_y\right)^2 + 4I_{xy}^2} \right) \tag{20}$$

The angle α_0 between the test axes x, y and the axes giving main second moments of the cross-section is calculated according to

$$\alpha_0 = -\text{arc}\tan\frac{I_{xy}}{I_1 - I_y}. \tag{21}$$

Table 3 shows that the largest rotation angle is $\pm 8^0$, and both $+8^0$and -8^0occur for carbon pillar. Different reasons could have caused the occurrence of this angle. Some of them are related to the physical process of deformation, distortion of the cross-section, while others are related to possible error during imaging. The latter seems more likely since distortion should be more pronounced for asymmetric tricot stitch rather than elliptic-shaped pillar stitch, while the rotation angles are higher for pillar stitch. For carbon pillar, initial data were recalculated to its main axes according to the formulae

$$x' = x\cos\alpha_0 - y\sin\alpha_0 \tag{22}$$

$$y' = x\sin\alpha_0 - y\cos\alpha_0 \tag{23}$$

and the strain values were recalculated in these main axes. Correction for axis rotation did not affect the results significantly: it can be seen from comparison to initial axes and to rotated axes that the strain values vary within 1 %. Consequently, possible error (up to several degrees) in rotating sequential images with respect to each other does not play a role in evaluating lateral strains.

Figs. 15 and 16 show the probability distribution curves for the tricot stitch and the chain stitch, respectively. For these distributions, bar graphs were constructed to show the number of fibers in proportion to the probability density, similarly for both the tricot and chain stitches. The constructed bar graphs clearly characterize the fiber distribution as a function of their distance from the center of the cross-section. As can be seen from Fig. 15a, in the initial unloaded state, the fibers are distributed more widely from the center, resulting in a more dispersed cross-sectional area. With an increase in the pre-tension level, the fibers tend to regroup and become concentrated closer to the center of the section. It is evident that the width of this probability distribution decreases accordingly. It should be noted, however, that no significant difference is observed between the 25% and 50% load levels. At the 75% level – that is, near the maximum load – the histogram bars become more elongated, indicating a higher degree of fiber compaction within the cross-section.

In contrast to the tricot stitch, the chain stitch does not exhibit such a pronounced scatter, as was observed in the figures described above. In this case, the fibers are more uniformly distributed across the cross-section, resulting in a relatively circular cross-sectional shape. As can be seen from Figs. 16b and 16c, only a slight

reorganization of fibers occurs, meaning that the cross-section compresses towards the center, but this has only a minor effect on the probability distribution. A similar pattern was also obtained for the glass fibers.

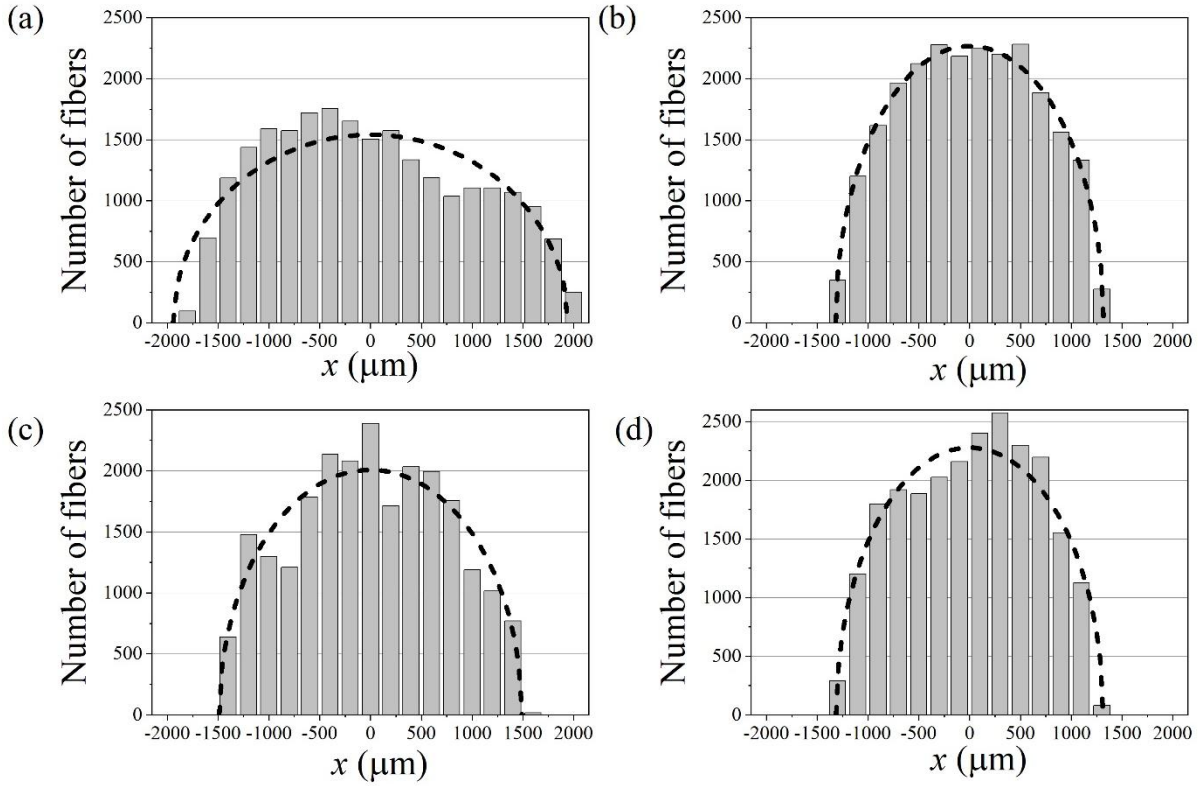


Fig. 15. Number of fibers (proportional to probability density) of the fiber distribution in tricot stitch carbon in the x (longer) direction. Experiment: bar graphs; theory: dash line. (a): loading 0%; (b): loading 25 %; (c): loading 50 %; (d): loading 75 %.

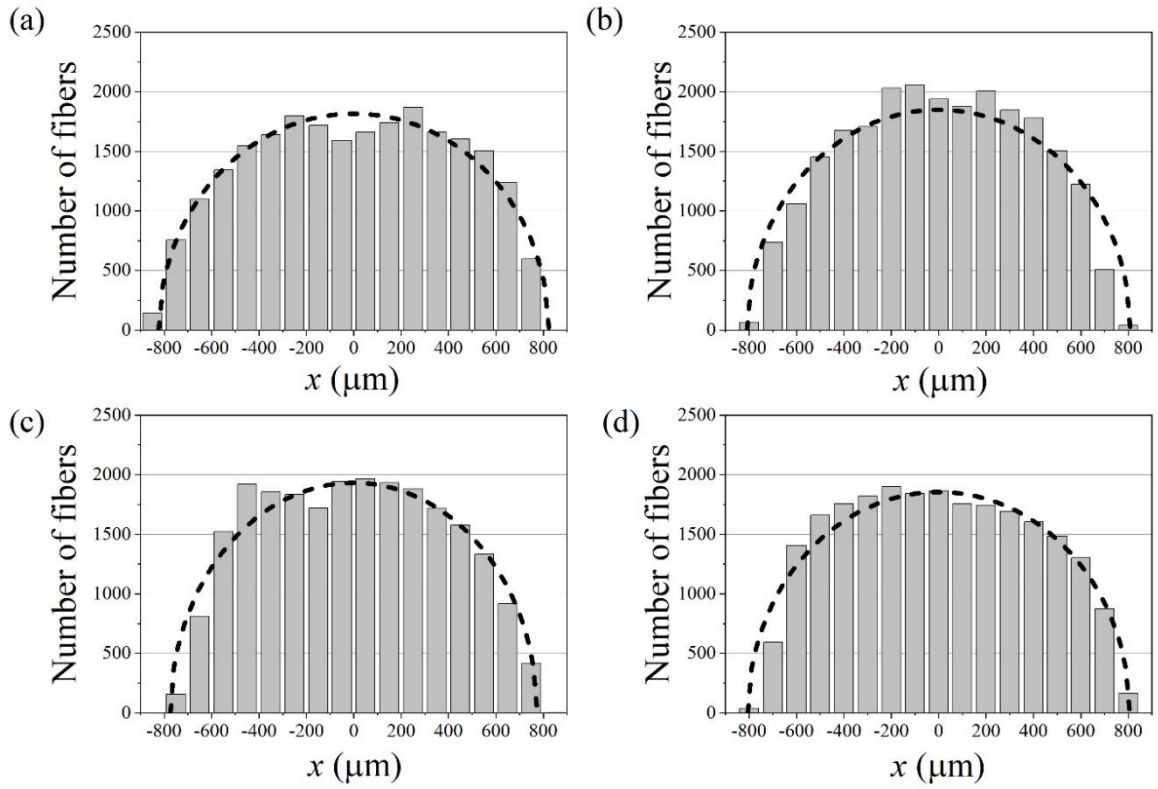


Fig. 16. Number of fibers (proportional to probability density) of the fiber distribution in pillar stitch carbon in the x (longer) direction. Experiment: bar graphs; theory: dash line. (a): loading 0%; (b): loading 25 %; (c): loading 50 %; (d): loading 75 %.

It is also useful to make a comparison with other textile rovings. Therefore, when loading the original roving from the bobbin (not in the fabric), a completely different characteristic occurs in the migration of filaments inside the section. In the absence of constraints caused by adjacent knitting yarns, the roving flattens to its maximum size. However, at first glance, its less efficient use in warp-knitted fabrics makes it possible to produce products of a much larger area and variety of shapes in comparison with the use of single rovings, for example, in windings.

Considering the results from the measurements of the cross-section parameters under loading, it is possible to predict the changes that affect the mechanical characteristics of the fabric. If the cross-sectional shape and contact length are reduced, the result is a loss of contact between the reinforcing fiber and matrix. The numerical dependence of these parameters on the loading degree makes it possible to evaluate the possible loss of contact and to choose the most suitable roving cross-section. The problems associated with the prestressing of fabrics in composites can also be solved. In a pre-stressed reinforcement, the cross-section will vary significantly. As a result, the mechanical characteristics will depend not only on the higher realization of mechanical properties owing to the increased strength, but also on the redistribution of the fiber within the section, leading to a lower efficiency in the properties, e.g., owing to interfibrillar friction.

4. Conclusions

In this work, the changes in the roving cross-section of warp-knitted fabrics composed of glass and carbon rovings with tricot and pillar stitch patterns were investigated. Optical micrographs of cross-sections of the warp-knitted fabric structures during loading were collected by image processing and fiber recognition in the roving cross-section. The changes in the roving cross-section of the prestressed rovings were considered in relation to four levels of loading.

It is shown that the stitch pattern exerted a significant effect on the roving cross-sectional shape. With increasing loading, the cross-sectional shape changes significantly in the case of the tricot stitch. In contrast to the fabric with tricot stitch, the cross-sectional shape of the fabric with pillar stitch slightly decreases with an increase in the applied load. A decreasing dependence on these characteristics was obtained with an increase in the level of prestress. A significant decrease in the calculated characteristics was observed in the initial stages of deformation (up to 25%).

To analyze the fiber distribution within the cross-section, a statistical processing of the measurement results was performed. Elliptical approximation was employed, and probability distribution curves were constructed for both the tricot and chain stitches. This statistical analysis provides a quantitative description of all changes occurring during fiber migration within the cross-section, as well as changes in the cross-sectional shape.

Acknowledgments

The research was funded by the Russian Science Foundation (project No. 25-29-00771).

References

1. Hu D. Basic concepts of prestressed concrete. In: Analysis and Design of Prestressed Concrete. Elsevier; 2022:1-13. https://doi.org/10.1016/B978-0-12-824425-8.00001-4

2. Peled A, Mobasher B, Bentur A. Textile Reinforced Concrete. CRC Press; 2017. https://doi.org/10.1201/9781315119151

3. Hutaibat M, Ghiassi B, Tizani W. Bond behaviour of prestressed basalt textile reinforced concrete. Constr Build Mater. 2024;438:137309. https://doi.org/10.1016/j.conbuildmat.2024.137309

4. Reinhardt H, Krüger M, Große C. Concrete prestressed with textile fabric. J Adv Concr Technol. 2003;1(3):231-239.

5. Bernat-Maso E, Gil L, Mercedes L, Escrig C. Mechanical properties of pre-stressed fabric-reinforced cementitious matrix composite (PFRCM). Constr Build Mater. 2018;191:228-241. https://doi.org/10.1016/j.conbuildmat.2018.09.210

6. Hong S, Park SK. Effect of prestress levels on flexural and debonding behavior of reinforced concrete beams strengthened with prestressed carbon fiber reinforced polymer plates. J Compos Mater. 2013;47(17):2097-2111. https://doi.org/10.1177/0021998312454318

7. Haas R, Quadflieg T, Stolyarov O. Analysis of reinforcement efficiency and microscopic characterization of glass and carbon roving geometry in prestressed concrete composites. J Compos Mater. 2021;55(23):3293-3305. https://doi.org/10.1177/00219983211013382

8. Hong J, Zhang S, Fang H, Xu X, Xie H, Wang Y. Structural performance of textile reinforced concrete sandwich panels under axial and transverse load. Rev Adv Mater Sci. 2021;60(1):64-79. https://doi.org/10.1515/rams-2021-0015

9. Nguyen XB, Tran MT, Vu XH, Ferrier E. Effect of the reinforcement ratio on the mechanical behaviour of textile-reinforced concrete composite: Experiment and numerical modeling. Open Eng. 2024;14(1). https://doi.org/10.1515/eng-2024-0086

10. Nahum L, Peled A, Gal E. The flexural performance of structural concrete beams reinforced with carbon textile fabrics. Compos Struct. 2020;239:111917. https://doi.org/10.1016/j.compstruct.2020.111917

11. Scholzen A, Chudoba R, Hegger J. Thin-walled shell structures made of textile-reinforced concrete. Struct Concr. 2015;16(1):106-114. https://doi.org/10.1002/suco.201300071

12. Hegger J, Curbach M, Stark A, Wilhelm S, Farwig K. Innovative design concepts: Application of textile reinforced concrete to shell structures. Struct Concr. 2018;19(3):637-646. https://doi.org/10.1002/suco.201700157

13. Hausding J, Engler T, Franzke G, Köckritz U, Cherif C. Plain stitch-bonded multi-plies for textile reinforced concrete. Autex Res J. 2006;6(2):81-90. https://doi.org/10.1515/aut-2006-060203

14. Ngo DQ, Vu VH, Nguyen HC. Experimental and numerical study on carbon textile reinforced concrete strengthening of pre-cracked reinforced concrete beams under sustained load. J Build Eng. 2026;122:115724. https://doi.org/10.1016/j.jobe.2026.115724

15. Yang T, Yang P, Zou Z, Ma P. Mechanical properties of warp-knitted metal mesh fabric under biaxial tension loading. Text Res J. 2021;91(11-12):1368-1379. https://doi.org/10.1177/0040517520981997

16. Ghorbani V, Jeddi AAA, Dabiryan H. Theoretical and experimental investigation of tensile properties of net warp-knitted spacer fabrics. J Text Inst. 2020;111(4):518-528. https://doi.org/10.1080/00405000.2019.1649579

17. Gao X, Yang X, Wu X, Ma P. An experimental investigation for the temperature effect on the bending properties of multiaxial warp-knitted composite. J Eng Fiber Fabr. 2020;15. https://doi.org/10.1177/1558925020915586

18. Xu S, Krüger M, Reinhardt HW, Ožbolt J. Bond characteristics of carbon, alkali resistant glass, and aramid textiles in mortar. J Mater Civ Eng. 2004;16(4):356-364. https://doi.org/10.1061/(ASCE)0899-1561(2004)16:4(356)

19. Du Y, Zhang M, Zhou F, Zhu D. Experimental study on basalt textile reinforced concrete under uniaxial tensile loading. Constr Build Mater. 2017;138:88-100. https://doi.org/10.1016/j.conbuildmat.2017.01.083

20. Du Y, Zhang X, Zhou F, Zhu D, Zhang M, Pan W. Flexural behavior of basalt textile-reinforced concrete. Constr Build Mater. 2018;183:7-21. https://doi.org/10.1016/j.conbuildmat.2018.06.165

21. Alamdar-Yazdi A, Heppler GR. Cross-sectional shapes of the yarn in cotton gray woven fabric. J Text Inst. 2011;102(3):248-262. https://doi.org/10.1080/00405001003703864

22. Barburski M, Masajtis J. Modelling of the change in structure of woven fabric under mechanical loading. Fibres Text East Eur. 2009;72(1):39-44.

23. Stolyarov O, Ershov S. Experimental study and finite element analysis of mechanical behavior of plain weave fabric during deformation through a cross-section observation. Mater Today Commun. 2022;31:103367. https://doi.org/10.1016/j.mtcomm.2022.103367

24. Anoshkin AN, Pisarev PV, Ermakov DA, Roman KV. Microstructural modeling and prediction of effective elastic properties in 3D reinforced composite material. Mater Phys Mech. 2022;50(1):89-106. https://doi.org/10.18149/MPM.5012022_7

25. Barburski M, Straumit I, Zhang X, Wevers M, Lomov SV. Micro-CT analysis of internal structure of sheared textile composite reinforcement. Compos Part A Appl Sci Manuf. 2015;73:45-54. https://doi.org/10.1016/j.compositesa.2015.03.008

26. Zhang Y, Zheng F, Liu X, et al. Siro false twist spun yarn structure and the knitted fabric performance. Text Res J. 2023;93(17-18):4096-4104. https://doi.org/10.1177/00405175231171167

27. Chiu SH, Chen JY, Lee JH. Fiber recognition and distribution analysis of PET/Rayon composite yarn cross sections using image processing techniques. Text Res J. 1999;69(6):417-422. https://doi.org/10.1177/004051759906900605